Visualization of Mixing Processes in a Heterogeneous Sand Box Aquifer

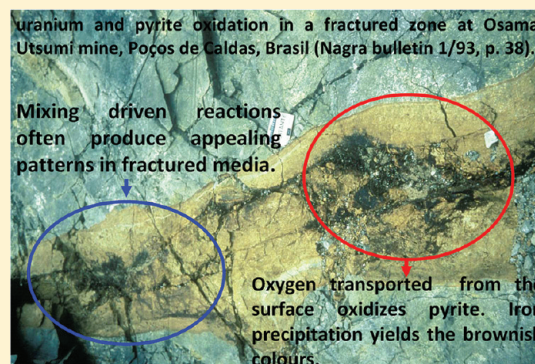Eduardo Castro-Alcalá,*,[†] Daniel Fernàndez-Garcia,[†] Jesus Carrera,[‡] and Diogo Bolster[§]

[†]Department of Geotechnical Engineering and Geosciences, Technical University of Catalonia (UPC), Barcelona, Spain
[‡]Institute of Environmental Assessment and Water Research (IDAEA-CSIC), Barcelona, Spain
[§]Department of Civil Engineering and Geological Sciences, University of Notre Dame, Notre Dame, Indiana, United States

Ⓢ *Supporting Information*

ABSTRACT: Mixing is increasingly recognized as a critical process for understanding and modeling reactive transport. Yet, mixing is hard to characterize because it depends nonlinearly on concentrations. Visualization of optical tracers in the laboratory at high spatial and temporal resolution can help advance the study of mixing processes. The solute distribution is obtained by analyzing the relationship between pixel intensity and tracer concentration. The problem with such techniques is that grain borders, light fluctuations, and nonuniform brightness contribute to produce noisy images of concentrations that cannot be directly used to estimate mixing at the local scale. We present a nonparametric regression methodology to visualize local values of mixing from noisy images of optical tracers that minimizes smoothing in the direction of concentration gradients. This is achieved by weighting pixel data along concentration isolines. The methodology is used to provide a full visualization of mixing dynamics in a tracer experiment performed in a reconstructed aquifer consisting of two materials with contrasting hydraulic properties. The experiment reveals that mixing is largest at the contact area of regions with different permeability. Also, the temporal evolutions of mixing and dilution rates are significantly different. The mixing rate is more persistent than the dilution rate during tracer invasion, and the opposite is true during flushing, which helps in understanding the complementary nature of these two measures.

uranium and pyrite oxidation in a fractured zone at Osama Utsumi mine, Poços de Caldas, Brasil (Nagra bulletin 1/93, p. 38).

Mixing driven reactions often produce appealing patterns in fractured media.

Oxygen transported from the surface oxidizes pyrite. Iron precipitation yields the brownish colours.

INTRODUCTION

Proper characterization of the mixing processes occurring in the subsurface is crucial for a comprehensive description of a large variety of biogeochemical problems, including cave formation, calcite precipitation and dolomization,[1−6] and chemical speciation and microbial reactions,[7−12] among others. What emerges from these works is that the rate of reactions, their location, and the conditions under which they occur all depend not only on chemistry but also on the rate of mixing.[13] Several measures of mixing can be found in the literature.[10,11,14,15] When transport can be fully defined in terms of conservative components (i.e., when all reactions are locally instantaneous and in equilibrium) and mixing of all solute species is locally controlled by diffusion (or dispersion), De Simoni et al.[16] showed that the reaction rate per unit volume of fluid, r, associated with a binary chemical system $\{c_1, c_2\}$ can be expressed as

$$r(\mathbf{x}, t) = F_{chem}F_{mix}, \quad F_{mix} = \nabla^T u \mathbf{D} \nabla u, \quad F_{chem} = \frac{\partial^2 c_2}{\partial u^2}$$

(1)

where u is the concentration of the conservative component, and $\mathbf{D}$ is the diffusion (hydrodynamic dispersion) tensor. This expression states that reaction rates are actually determined by the product of two terms: one term (F_{chem}) that only depends on the speciation of the reactive species and another term (F_{mix}) that measures mixing, caused by the joint effect of the local concentration gradients and diffusion (dispersion). This measure of mixing appears repeatedly in the literature and will be the subject of this paper. Kapoor and Gelhar[17] demonstrated that the variance of concentrations follows an Advection−Dispersion Equation (ADE) with an F_{mix} related sink term that is responsible for smearing the concentrations in aquifers. Similarly, Sanchez-Vila et al.[18] found that the probability density function of the concentrations of reactive and conservative species satisfies a nonlocal ADE with a source term related to F_{mix}. The probability of occurrence of "mixed" concentrations was found to increase with F_{mix}. This measure of mixing is also included in the dilution index ratio proposed by Kitanidis,[19] which is closely related to entropy. It is a measure that quantifies the degree of dilution in a system reflecting the apparent volume occupied by the solute, aiding one to distinguish between macrodisperive spreading (effective
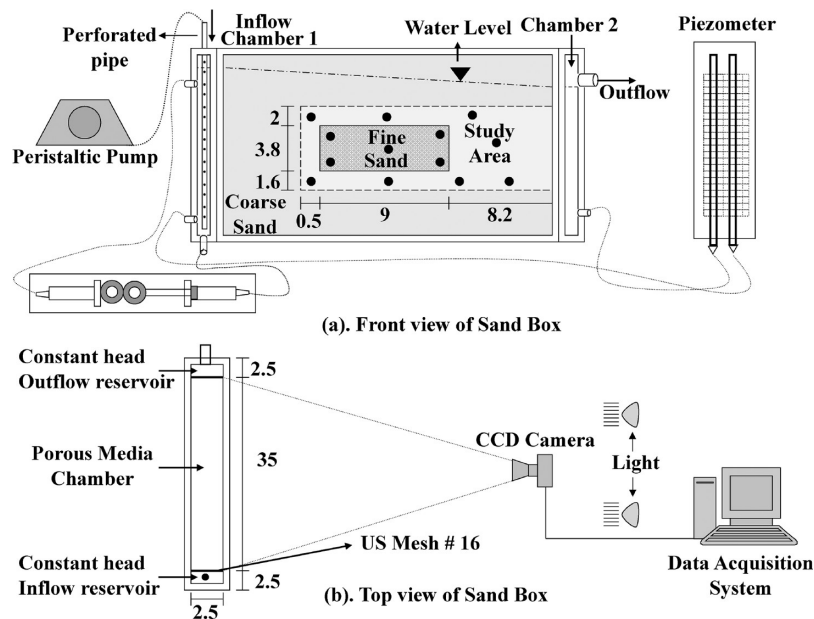
Figure 1. Schematic experimental setup of the sand box: (a) front view; (b) top view. Measurements are in centimeters.

plume size) and dilution. Kitanidis[19] defines the degree of dilution as being quantified by

$$E(t) = \exp\left(-\int_v p\ln(p)d\mathbf{x}\right), \quad p(\mathbf{x}, t) = \frac{u(\mathbf{x}, t)}{\int_v u(\mathbf{x}, t)d\mathbf{x}}$$

$$(2)$$

Instead, F_{mix} describes mixing at the local scale, which is directly related to the reaction rates occurring at a given location and time. Global mixing (i.e., the integral of over the entire domain) is proportional to the dissipation rate time derivative of the global concentration variance, regardless of the type of flow field.[20]

In real field settings, the gradients of concentrations involved in the definition of F_{mix} are highly influenced by the natural variability of aquifer properties. In general, the erratic velocity fields typically obtained in natural aquifers produce highly distorted solute plumes that enhance mixing, (e.g., refs 21 and 22). Although the relationship between physical heterogeneity and mixing remains undefined, it is well-known that the advection–dispersion equation provides a poor representation of mixing at all scales. This has been shown in homogeneous column experiments[15] and in numerical simulations and stochastic analysis of solute transport performed in heterogeneous media.[21,22]

The lack of an appropriate quantification of mixing compromises the reliability of reactive transport simulations. Thus, more fundamental studies of mixing through laboratory experiments are needed. A promising laboratory method for understanding mixing is tracer visualization at high spatial and temporal resolutions. This method consists of visualizing the migration of an optical tracer injected into a porous medium. A full picture of the solute distribution is obtained by analyzing the relationship between pixel intensity and tracer concentration in time and space. The problem with these techniques is that the roughness and geometric properties of the porous media, light fluctuations, and variations in brightness due to nonuniform light sources, among a variety of other problems, produce noisy estimates of concentrations. Several attempts

have been made in the past to reduce this noise. McNeil et al.[23] proposed to segment the image optically, Rahman et al.[24] used both a geometric correction and color calibration, Schincariol et al.[25] suggested a general median smoothing to 3 × 3 pixels to reduce the noise associated with glass bead sizes, and Konz et al.[26] filtered the image using a window averaging technique consisting of 10 × 10 pixels. All these approaches were designed to improve the estimates of concentrations but none of them are well suited to directly estimate mixing. A complete representation of mixing requires detailed knowledge of concentration gradients, which cannot be directly estimated from noisy images.

The objective of this paper is to present a methodology aimed at fully visualizing mixing from light intensity images of optical tracers. This methodology is then applied to visualize the mixing dynamics occurring in a tracer experiment performed in a heterogeneous sand-box aquifer.

■ EXPERIMENTAL PROCEDURE

Sand Box. The tracer experiment was conducted in an unconfined heterogeneous aquifer reconstructed in the laboratory. The sand distribution in the tank consisted of a rectangular inclusion of fine sand (low permeability) embedded in an otherwise highly permeable coarse sand. The objective of this particular distribution was to visualize and quantify the mixing dynamics occurring at the interface between two distinct materials with contrasting hydraulic properties.

The sand box containing the aquifer is a quasi two-dimensional vertical tank of length 36.5 cm, height 27 cm, and width 2.5 cm, fully made of transparent plexiglass. The sand box was divided into three distinct chambers. Figure 1 shows a sketch diagram of the experimental setup. The central chamber is 32.5 cm long and contained the reconstructed aquifer. Two stainless steel meshes US#16 separated the influent and effluent chambers from the central flow chamber. The influent and effluent chambers served to prescribe the head boundary conditions needed to run the tracer experiment.

A sieve analysis determined that the sand was poorly graded with a coefficient of uniformity of 1.2 and 1.25 for the coarse

and fine sands, respectively. Grain diameters range from 1.0 to 1.2 mm for the coarse sand, and from 0.4 to 0.6 mm for the fine sand. A constant head permeameter cell was used to determine the hydraulic conductivity of the sands, obtaining 1060 m/day and 67.5 m/day for the coarse and fine sand, respectively. The tank was packed under fully saturated conditions layer by layer to avoid trapping of air and minimize segregation. The porosity was estimated gravimetrically as 0.4.

Tracer Experiment. Red Rhodamine B (Panreac) was injected into the sand-box aquifer. This compound can effectively be considered as a conservative tracer because it neither adsorbs nor degrades in clean quartz sand. The tracer experiment proceeded as follows. First, water was pumped into the aquifer at a constant rate of 49 mL/min through a perforated vertical pipe into chamber 1. This produced a constant head of 24.15 cm at the inflow reservoir and 23 cm at the outflow reservoir. Once steady-state conditions were achieved, Rhodamine B was continuously injected into the aquifer at a concentration of 200 mg/L for 42 min at the same flow rate. After this, the tank was flushed with freshwater. The start and stop of tracer injection were carefully executed to minimize head perturbations. For this, two connected sets of syringes were employed to rapidly extract and replace the fluid in chamber 1 with the desired solution (with a transient of roughly 5 s).

Image Acquisition. The plexiglass structure of the sand box permits visualization of the migration of the optical tracer without a disturbance of the mixing dynamics inside the aquifer. Many authors have utilized optical tracers to visualize and quantify solute concentrations in synthetic aquifers.[23−27] Light transmission or reflected light are the two techniques used to obtain map concentrations. Here, we choose reflected light for image analysis so that we may analyze a generic nontransparent sand material with different mineralogy and texture. We tested four different types of light sources (incandescent, halogen, fluorescent, and LEDs). Best results in terms of sensitivity, temperature, and fluctuations were obtained with LEDs. Some LEDs properties are uniform spectral power distribution (from 380 to 780 nm), constant light color, good heat dissipation, higher luminous flux, and a better luminous efficacy. Two LED light sources were placed at a distance of 20 cm from the tank.

A CCD camera (AVT Guppy F-080B/C) was used to continuously record the red (R), green (G), and blue (B) color images of the tracer experiment. A computer program (AVT SmartView v1.7.2) controlled the image acquisition and transfer of information to a computer. We set all parameters manually (relative aperture F5.6, shutter speed 1/30). These parameters were the same for both calibration and image processing of the experiment. Images were acquired every 6 s during the whole experiment. The camera and the tank were fixed to a metal structure placed inside a black room to fully control the light intensity emitted to and reflected from the tank. The black room was located inside a temperature controlled lab and ventilated with fans to ensure a constant temperature. The spatial resolution of the camera was 1024 × 728 pixels. Each pixel represents an area of 0.32 × 0.32 mm^2 and has a color resolution of 8 bits. Thus, the RGB color channels range linearly between 0 and 255 in terms of values of intensity.

Image Processing. The concentration interpretation of optical tracers is based on the relationship between light intensity and tracer concentration.[15,23−26] The application of such a relationship in porous media can be cumbersome because light intensity is affected by factors other than

absorption and reflection of a light ray passing through a fluid with tracer concentrations. In particular, the light rays are also influenced by the roughness and geometric properties of the sand grains, fluctuations in the source light, and brightness variations due to nonuniform lightning that introduce noise.

Methodology. The procedure we used for image processing follows five principle steps: [1] capture the image in raw data and convert it to 8-bit BMP images; [2] select the channels most sensitive to the tracer; [3] determine the relationship between light intensity and concentrations for each image pixel; [4] use the light intensity relationships to map concentrations; and [5] reconstruct concentrations and mixing from the noisy images of concentrations. Because our objective is to examine the occurrence of mixing at the interface between materials, we restricted our image processing analysis to the study area depicted in Figure 1.

Selection of a Color Channel. Preliminary tracer tests revealed that substantial differences exist between the signals in each of the three color channels. Figure 2 shows the channel
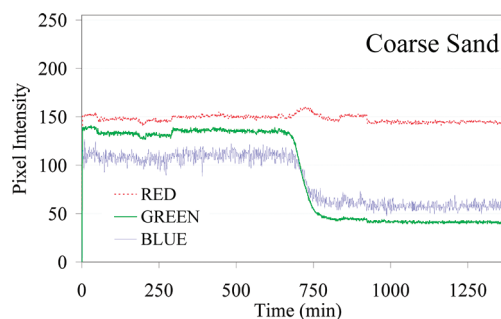
Figure 2. Sensitivity of light intensity during Rhodamine injection for one representative pixel associated with coarse sand.

signal observed for the red, green, and blue channel as a function of time during the tracer experiment. The green channel was seen to be the most sensitive, likely because the maximum absorption wavelength of Rhodamine B (565 nm) is close to the wavelength of the excitation light (545 nm). Figure 2 also shows that the green channel provides a less noisy response than the blue and red spectrum. Based on this, we chose to work with the green channel signal.

Relationship between Light Intensity and Concentrations. To account for the spatial variations of light intensity and the influence of an underlying nontransparent porous medium, we analyzed the relationship between light intensity and concentrations pixel by pixel.[26] This was found crucial for analyzing this type of experiments. These relationships were calibrated before running the experiment by injecting 11 known solutions of Rhodamine B into the sand-box aquifer (0, 10.13, 19.79, 30.47, 38.7, 8.83, 87.86, 120, 147.8, 179.19, 199.87 mg/ L). These solutions were independently injected into the tank from low to high concentrations. For each solution, a continuous injection was performed until a steady-state image of reflected light intensity was obtained. The resulting images $I_1(\mathbf{x}),...,I_{11}(\mathbf{x})$ constituted the reference light intensity for the given solution of Rhodamine B. The final relationship was

obtained by using a piece-wise linear model of the data points as

$$C(I; \mathbf{x}) = C(I_i; \mathbf{x}) + \frac{C(I_{i+1}; \mathbf{x}) - C(I_i; \mathbf{x})}{I_{i+1}^*(\mathbf{x}) - I_i^*(\mathbf{x})}$$

$$\times (I^*(\mathbf{x}) - I_i^*(\mathbf{x})), \quad I^*(\mathbf{x}) \in [I_i^*(\mathbf{x}), I_{i+1}^*(\mathbf{x})] \quad (3)$$

where $C(I;\mathbf{x})$ is the concentration of Rhodamine B at location $\mathbf{x}$ for a light intensity I, and I^* is a normalized light intensity, defined as $I^*_i = I_i/I_i^{\,0}$. The light intensity I^0 is the light intensity of a blank image obtained under steady-state flow conditions before the injection (taken as the average over 60 min). This normalization aims to remove any small temporal variations in the energy supply that can substantially affect light intensity.[26] Figure 3 shows the calibration curves obtained for
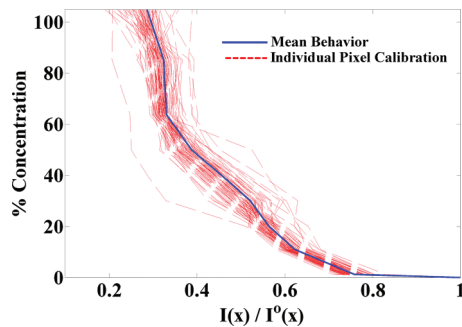
Figure 3. Calibration curves on concentration against normalized pixel intensity for representative pixels located in both the high and low permeability zones.

several pixels in the study area. The large width of the ensemble illustrates the importance of calibrating this relationship pixel by pixel for this type of experiment.

Reconstruction of Mixing from Noisy Images. Concentration fields, $u(\mathbf{x},t)$, can be estimated from noisy images $C(I;\mathbf{x})$ using a suite of parametric and nonparametric methods.[28] All of them involve either local regressions, filtering of noise, or both. A shared drawback is that they may produce some degree of oversmoothing or bias of the concentration field and the mixing rate F_{mix}. To minimize this effect, we propose here a methodology that attempts to obtain the best of two existing methods:

- The *Steering Kernel Regression* method (SKR) of Takeda et al.,[29] which is based on weighting concentration measurements in the direction of concentration isolines, ensures that no smoothing is produced in the concentration gradient direction. Although this method provides high quality images, it does not provide a clear way to optimally define smoothing parameters.
- The *weighted kernel density estimation* method (wKDE) which is capable of automatically selecting the optimal level of smoothing, but fails to optimally orient the kernel function. As a result gradients may be smoothed out in areas where concentration gradients are not aligned with the mean flow direction.

The proposed approach consists of two stages. During the first stage, the wKDE method is applied to small areas of the image, where concentration isolines are aligned with the x and/or y axis, and where the wKDE method works well.[30] The size of these areas is (100×100 pixels) and their centroids are shown in Figure 1 as black circles. The mixing rate, F_{mix}^{wKDE}, is

evaluated at these areas. At the second stage, the more sophisticated data-adaptive SKR method is used, selecting its smoothing parameters so as to match F_{mix}^{SKR} with F_{mix}^{wKDE} as closely as possible. Details of both methods are outlined below. Optimality of the wKDE method is presented in the Supporting Information.

Weighted Kernel Density Estimation. Let $p = \phi u/M$ be the normalized concentration field of an image recorded at time t, where M is the mass of tracer at time t, known from the experimental mass balance of the optical tracer, and ϕ is the porosity. Then, the problem of reconstructing mixing is reduced to the estimation of p and its gradient $\nabla p = [p_x p_y]^T$ given a sample of pixel values. The focus here will be on

$$F_{mix}^{wKDE} = \left\| \nabla u \right\|^2 = M^2 \left\| \nabla p \right\| / \phi^2 \quad (4)$$

which is related to local reactions by eq 1. Estimation of p and ∇p can be optimized easily for 1D problems. Fernàndez-Garcia and Sanchez-Vila[30] generalized the 1D optimal methods by viewing concentrations as a cumulative probability distribution function and using the definition of the conditional density function $p(x,y) = p(y|x)p(x) = p(x|y)p(y)$, where $p(x|y)$ and $p(y|x)$ are the conditional density functions, and $p(x)$ and $p(y)$ are the marginal density functions, which leads to

$$u(x, y, t) = M/\phi \sqrt{p(y|x)p(x)p(x|y)p(y)} \quad (5)$$

$$F_{mix}^{wKDE}(x, y, t) = M^2 (p(y|x)p_x(x)p_x(x|y)$$
$$p(y) + p(x|y)p_y(y)p_y(y|x)p(x))/\phi^2 \quad (6)$$

where p_x and p_y denote the derivatives of the corresponding univariate probability density functions. Let us consider for instance the marginal density functions $p(x)$ and $p_x(x)$. The wKDE estimators of these marginal probabilities are obtained from the normalized pixel data $p_i = p(\mathbf{x}_i)$ $i = 1,...,n$ as

$$p(x) \approx \sum_{i=1}^{n} \frac{p_i}{h_0} K\left(\frac{x_i - x}{h_0}\right),$$

$$p_x(x) \approx \sum_{i=1}^{n} \frac{p_i}{h_1^2} K'\left(\frac{x_i - x}{h_1}\right) \quad (7)$$

where K is a weight function, chosen as a zero mean and unit variance Gaussian distribution, K' is its derivative, and h_0 and h_1 are, respectively, the levels of smoothing for p and p_x. Using the mean integrated squared error criterion to evaluate the expected error of these estimators, the optimal supports are[31]

$$h_0 = \left(\frac{R(K)}{(\mu_2(K))^2 R(p'')n} \right)^{1/5},$$

$$h_1 = \left(\frac{3R(K')3!^2}{4(\mu_3(K'))^2 R(p''')n} \right)^{1/7} \quad (8)$$

where $R(g)$ and $\mu_n(g)$ are the L^2-norm and the nth-absolute moment of g. These optimal estimates involve the unknown function p, which needs to be further estimated. To this end, we used the plug-in algorithm described in ref 31. The use of eqs 5−8 to estimate mixing has been already thoroughly tested against analytical solutions and shown to outperform traditional

3231

dx.doi.org/10.1021/es201779p | *Environ. Sci. Technol.* 2012, 46, 3228−3235

methods[30] for concentration fields described in terms of particles. The fields here are not made up of particles, however, this limitation can be overcome by expanding the sample data p_i in terms of constant mass particles.[32] That is, prior to the reconstruction of F_{mix}^{wKDE}, a new image was generated by uniformly distributing n_i pixel values of equal weight, $p_i = 1/N$, in each pixel cell according to $n_i = p(\mathbf{x},t)N$, where N is the total number of data points used ($N = 50\,000$) in the specific area.

Steering Kernel Regression. In nonparametric regression, the measured normalized concentrations are expressed as a local Taylor expansion around the estimation location $\mathbf{x}$ plus a noise term. Assuming a quadratic form of the regression model

$$p_i = \beta_0 + \beta_1 x'_i + \beta_2 y'_i + \beta_3 x'^2_i + \beta_4 x'_i y'_i + \beta_5 y'^2_i$$
$$+ e_i, ..., \quad i = 1, ..., n \tag{9}$$

where e_i is an independent and identically distributed zero mean noise value, $\mathbf{x}'_i = \mathbf{x}_i - \mathbf{x}$ is the distance from the estimation location, β_0 is the estimated pixel value at $\mathbf{x}$, $[\beta_1,\beta_2]^T$ its corresponding gradient and so on. In matrix form, this is simplified to

$$\mathbf{p} = \mathbf{Xb} + \mathbf{e},$$

$$\mathbf{X} = \begin{pmatrix} 1 & x'_1 & y'_1 & (x'_1)^2 & x'_1 y'_1 & (y'_1)^2 \\ \cdots & \cdots & \cdots & \cdots & \cdots & \cdots \\ 1 & x'_n & y'_n & (x'_n)^2 & x'_n y'_n & (y'_n)^2 \end{pmatrix} \tag{10}$$

where $\mathbf{b} = [\beta_0,\beta_1,\beta_2,\beta_3,\beta_4,\beta_5]^T$, $\mathbf{p} = [p_1,...,p_n]^T$, and $\mathbf{e} = [e_1,...,e_n]^T$. The regression parameter vector $\mathbf{b}$ is typically obtained by minimizing the weighted sum of squared residuals, i.e., SSE $= \mathbf{e}^T\mathbf{We}$, where $\mathbf{W}$ is a given weight matrix. The solution of this optimization problem is

$$\mathbf{b} = (\mathbf{X}^T\mathbf{WX})^{-1}\mathbf{X}^T\mathbf{Wp} \tag{11}$$

Because $\mathbf{b}$ and the regression function are expressed as a local weighted average of the data, the coefficients multiplying $\mathbf{p}$ in eq 11 can be denoted as equivalent weights. Nonparametric regression evaluates $\mathbf{b}$ at the estimation location $\mathbf{x}$ from only nearby data. A natural way to do this is to give nearby samples higher weight than samples further away so that

$$\mathbf{W} = diag\{K(\mathbf{x}'_1), ..., K(\mathbf{x}'_n)\} \tag{12}$$

where K is a weight function typically assumed as a Gaussian kernel,

$$K(\mathbf{x}'_i) = \frac{1}{2\pi\sqrt{\det(\mathbf{H}_i)}}\exp\left[\frac{\mathbf{x}'^T_i \mathbf{H}_i^{-1}\mathbf{x}'_i}{2}\right] \tag{13}$$

and $\mathbf{H}$ is the smoothing matrix. Whenever $\mathbf{H}$ is constant and does not depend on data values, the quality of the reconstruction in areas with complex geometries is low. To solve this problem, Takeda et al.[29] proposed to locally rotate and scale $\mathbf{H}$ to ensure that weight is concentrated along concentration isolines

$$\mathbf{H}_1^{-1} = \frac{1}{\mu^2}[\overline{\nabla u \nabla^T u}]_{\mathbf{x}=\mathbf{x}_i} \tag{14}$$

where the overbar stands for averaging over the pixels adjacent to $\mathbf{x}_i$, and μ is a global smoothing parameter. This filter is nonlinear because $\mathbf{H}_i$ depends now on the solution through ∇u. Therefore, its application is iterative. Figure 4 shows the maps
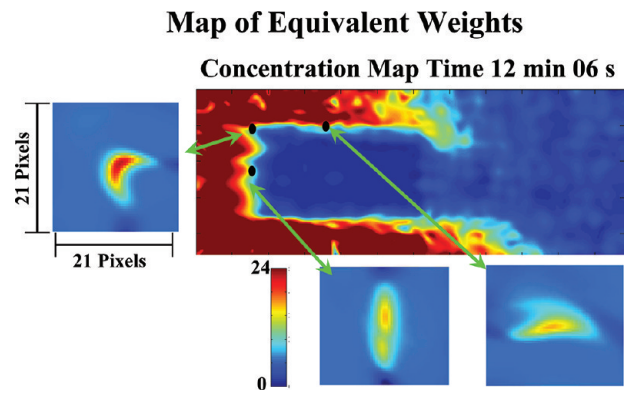
Figure 4. Map of equivalent weights used to calculate concentrations and concentrations gradients in eqs 7, 8, and 9 associated with three different pixels located within the mixing zone.

of equivalent weights obtained for three different pixels located in the mixing zone at time 12 min 6 s. Remarkably, these weights are able to adapt themselves to the presence of fine sand, even at the corner boundary, which ensures that little weight is given to concentration values inside the fine sand, thus preventing the smoothing of gradients. The mixing property can be finally estimated as

$$F_{mix}^{SKR} = \left\|\nabla u\right\|^2 = M^2(\beta_1^2(x, y) + \beta_2^2(x, y))/\phi^2 \tag{15}$$

The global smoothing parameter μ is chosen so as to obtain $F_{mix}^{SKR} \approx F_{mix}^{wKDE}$ at the selected areas during the first stage. We found that a value of μ equal to 3.6 pixels with 4 iterations provided optimal results.

■ RESULTS

We applied the kernel regression image processing techniques described in Experimental Procedure to the experimental setup in Reconstruction of Mixing from Noisy Images to map concentrations as well as mixing. Whereas the acquired images capture the full experimental setup, we focus our analysis and discussion only on the study area highlighted in Figure 1, which incorporates the boundaries between materials of contrasting permeability. Images were acquired every 6 s during both the initial 42 min of Rhodamine injection and the following 42 min of flushing with freshwater. Initially the tank is filled with freshwater that has zero Rhodamine content. Figure 5 shows the results obtained at 16 min and 54 s after injection. Here, the results of our proposed methodology are compared with those obtained directly from the calibrated images (nonfiltered data) and those obtained using a moving window average technique (MWA), which is the standard technique used in previous visualization experiments.[25,26] It consists simply of averaging the pixel values over a moving window. The gradients needed to estimate mixing in these cases were approximated by finite differences. We consider two possible windows consisting of 11 × 11 pixels and 51 × 51 pixels. The first window resembles previous studies to estimate concentrations.[26] The other provides a sufficiently smooth image with negligible noise. Although at first sight the 11 × 11 MWA provides reasonable images of concentrations, their local fluctuations are still too high to estimate mixing properly. On the contrary, the 51 × 51 MWA shows zero noise but at the expense of substantially oversmoothing mixing. Our proposed methodology is able to eliminate most of the fluctuations while still providing an
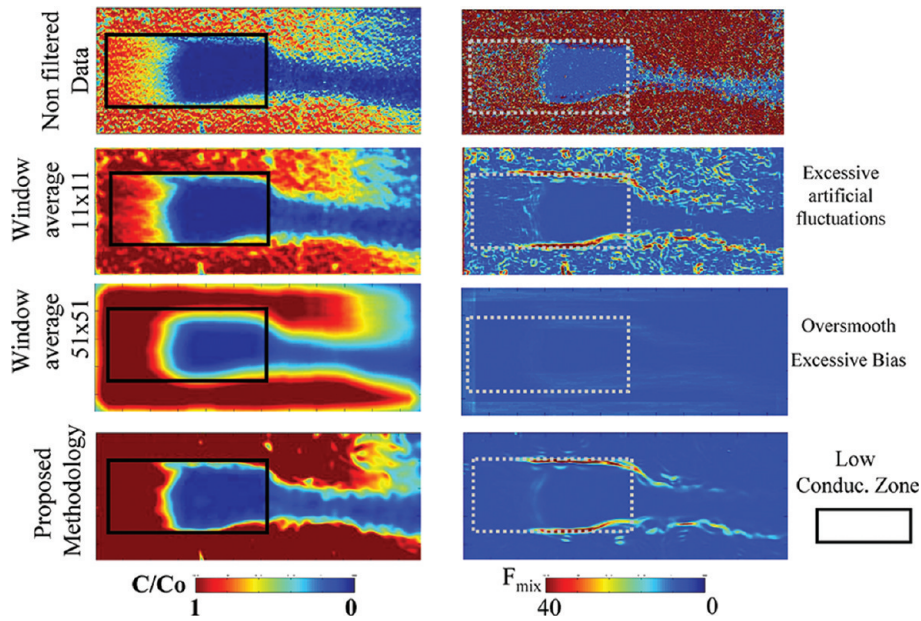
Figure 5. Image map of concentrations (left-hand side) and mixing (right-hand side) obtained at time 16 min and 54 s for different methods: (1) nonfiltered data; (2) 11 × 11 moving window average; (3) 51 × 51 moving window average; (4) proposed methodology.

adequate description of mixing. The ability to visualize concentrations and mixing so clearly using our iterative optimal kernel algorithm highlights the strength of the algorithm for these types of experiment.

The typical evolution of the concentration field by the injection and flushing is shown in Figure 6 over the entire
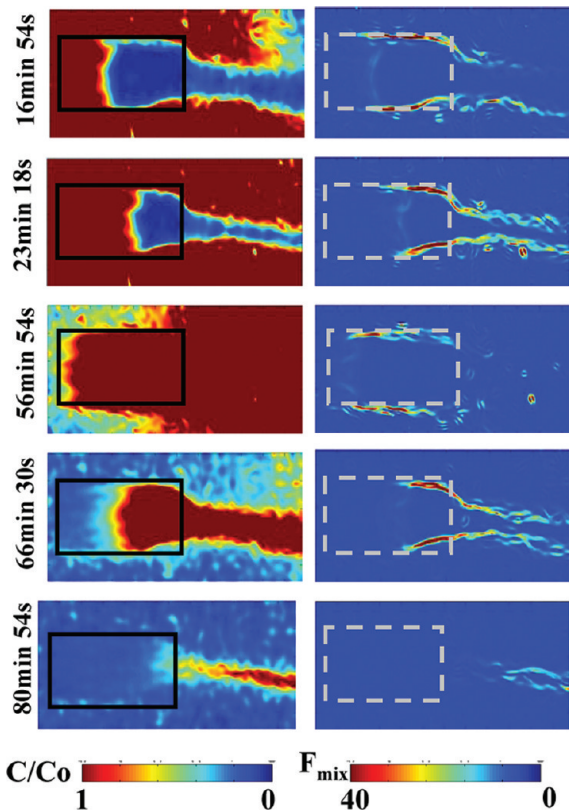
Figure 6. Temporal evolution of concentrations (left-hand side) and mixing (right-hand side) during the initial 42 min of Rhodamine injection and the following 42 min of flushing with freshwater.

course of the experiment. The tracer takes 7.2 min to arrive to the low-permeability sand inclusion and another 26.63 min to actually occupy the fine sand. The tank is completely full after 40 min. At early times the effect of macrodispersive spreading is evident as contaminant travels through the high permeability zones quickly, taking much longer to enter the low permeability zone, highlighting visually the fundamental difference between mixing and spreading. This causes strong gradients (particularly in the transverse direction) at the interface between the two materials. While the tracer takes relatively little time to cross the tank through the high permeability areas, it takes much longer for the tank to completely fill with Rhodamine due to the slower processes associated with the low permeability zone. This is strongly reminiscent of the mobile/immobile concepts often used in multirate mass transfer type models which have been relatively successfully extended to mixing driven reactions.[33] It is also important to highlight that the region directly downstream of the low permeability inclusion looks somewhat like a wake in that it takes a long time to fill and that strong transverse gradients persist here also. In this region, the solute traveling across the high permeability area in the tank is able to mix with an almost stagnant freshwater that still resides behind the inclusion.

The flushing process that begins after 42 min is qualitatively similar to the initial injection period, although a close look at the images in Figure 5 indicates some small differences. For instance, remaining fluctuations, manifested by hot round spots in the mixing image, are distributed in a different manner during the injection and flushing period. This can likely be attributed to the shape of the calibration curve, where high concentrations are more sensitive to light intensity. Thus, more noise is always observed in areas filled with Rhodamine. We note that the optimality of μ is based on a global criterion and therefore some local artificial fluctuations may still be produced.

These strong transverse gradients have significant implications with regard to reactive transport. As highlighted in the Introduction and mathematically illustrated in eq 1 the rate of reaction is directly proportional to the gradient squared.

Therefore, from Figure 6 we can infer that the regions of greatest reaction are not just at the mixing front advancing in the direction of flow as would be the case for a homogeneous medium, but specifically along interfaces between zones of differing permeability. This result is consistent with geological observations such as the formation of Mississippi Valley Type deposits[34] or permeability enhancement at the base of weathering fronts in plutonic rocks.[35] From the mixing images it is immediately obvious that these transverse gradients are dominant and that peak reaction rates are most likely to occur at interfaces with high permeability contrast. This in turn agrees with previous comments that transverse mixing is a fundamental driver of hydrogeochemical reactions, (e.g., refs 12 and 35).

Along with the local rate of mixing we can also estimate a global measure of mixing, which may be of more interest at the large scale. To this end, we use a global measure of mixing that is the integral of the concentration gradient squared over the study area

$$R_{mix}(t) = \int F_{mix}(\mathbf{x}, t)d\mathbf{x} \tag{16}$$

Figure 7 compares our result of R_{mix} with those obtain using the nonfiltered data and MWA technique. Results highlight that
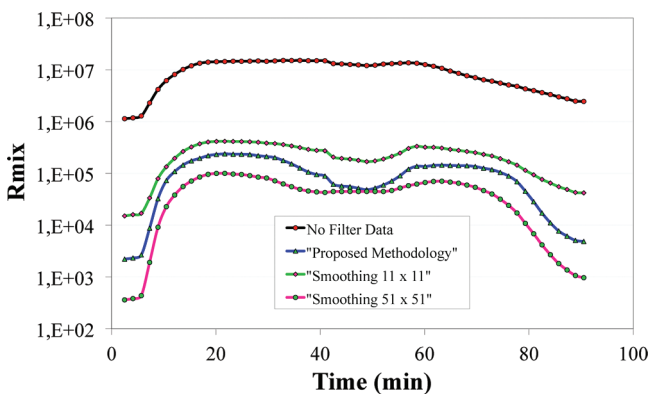

Figure 7. Comparison of the global mixing measure R_{mix} with MWA using a window of 11×11 and 51×51 pixels.

the artificial gradients introduced by the inherent noise of a nonfiltered image render meaningless results. This is not completely solved by using MWA techniques, which fail to reproduce the mixing valley induced by flushing the system with freshwater after the injection (time = 42 min).

As mentioned in the introduction, the dilution index E can also be used to quantify the degree of mixing. To understand what controls the rate of dilution of a solute in time, Kitanidis[19] proposed to evaluate the rate of change of the logarithm of the dilution index

$$R_E(t) = \frac{d\ln(E)}{dt} \tag{17}$$

Figure 8 shows R_E and R_{mix} for our tracer test. For early times, the distortion of the concentration field associated with the advection field causes the dilution rate to decrease with time with respect to the initial homogeneous well-mixed behavior. The minimum dilution rate (time = 7.3 min) occurs when the propagating front comes in contact with the low transmissivity zone. After that, from time = 7.3 min onward, strong vertical concentration gradients begin to form and there
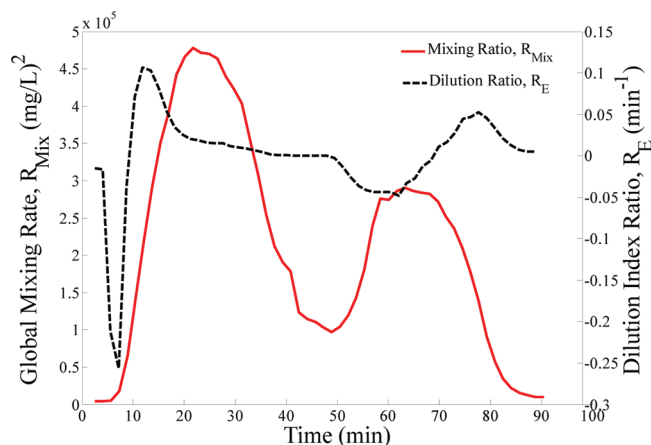
Figure 8. Temporal evolution of global mixing rate R_{mix} and dilution index rate R_E.

is a rapid increase in both the dilution ratio R_E and the global mixing rate R_{mix}. Both measures of mixing start increasing over the same time, but with substantially differing late-time behavior after the hump. That is, global mixing R_{mix} shows a more persistent effect with time since strong transverse gradients can continuously occur over the entire interface between materials. While the rate of volume occupied by solute undergoes a sudden hump when the tracer rapidly passes through the high-permeability zone, the concentration gradients persist until the tracer is able to finally occupy the low-permeability zone, later on, due to slow advection. Remarkably, the peak of R_{mix} occurs at time = 23 min, right when the solute has partially filled the low permeability area through slow advection and is able to further mix with the almost stagnant freshwater residing behind the inclusion.

Interestingly, the behavior of R_E and R_{mix} is different. While the dilution rate effectively measures the rate of change of the plume volume, which is very high during injection until the solute tracer reaches the low permeability region, this low permeability region generates strong gradients that enhance mixing over larger periods of time. The opposite occurs during flushing. The tracer lagging behind slows down the dilution rate until it is fully washed out. As a result R_E lags behind R_{mix} during flushing. This observation highlights that the two quantities are different but complementary.

■ CONCLUSIONS

The understanding of mixing processes is one of the current major challenges in subsurface hydrology. Tracer visualization is a convenient technique that is typically used to analyze processes in the laboratory. However, these techniques typically provide noisy images that only reliably quantify concentrations. They cannot be used to directly quantify mixing as this depends strongly on concentration gradients, which are very sensitive to noise. This article presents a novel methodology to overcome these problems. They can be used to investigate reactive transport processes under a variety of hydraulic and chemical conditions. The method is applied to visualize the local mixing processes that occur during the injection and flushing of tracer in a heterogeneous porous medium. Several important conclusions should be highlighted from this work. First, we have shown that while traditional image processing techniques do not provide proper mixing estimates, our optimal methodology can actually depict local mixing processes. Moreover, the

experiment demonstrates that transverse gradients can be dominant at interfaces with high permeability contrasts within aquifers as well as in areas of relatively low velocity. As a result, regions of greatest reactions should not be expected only at the mixing front advancing in the direction of flow, as would be the case for a homogeneous medium, but also along interfaces between zones of differing permeability. The experiment was also used to analyze the temporal evolution of two well-known mixing indices, i.e., the dilution index ratio and the global mixing rate. The peak of dilution was seen to occur relatively quickly after injection when the plume was most distorted by the spatially varying velocity field. In contrast, the peak of the global mixing rate occurred later when slow advection and mixing with stagnant water were the most active transport mechanisms.

■ ASSOCIATED CONTENT

Ⓢ Supporting Information

Detailed information of the optimality of the wKDE. This information is available free of charge via the Internet at http://pubs.acs.org/.

■ AUTHOR INFORMATION

Corresponding Author

*E-mail: eduardo.castro@upc.edu; phone: (34)93 4016852; fax: (34) 93 4017251.

■ REFERENCES

(1) Runnels, D. *J. Sediment. Petrol.* **1969**, *39*, 1188−1201.

(2) Hanshaw, B.; Back, W. *J. Hydrol.* **1979**, *43* (20), 287−312.

(3) Raeisi, E.; Mylroie, J. *Carbonates Evaporites* **1979**, *10*, No. 10.1007/BF03175405.

(4) Ayora, C.; Taberner, C.; Saaltink, M.; Carrera, J. *J. Hydrol.* **1998**, *209*, 346−365.

(5) Willingham, T.; Werth, C.; Valocchi, A. *Environ. Sci. Technol.* **2008**, *49* (2), 3185−3193.

(6) Zhang, C.; Dehoff, K.; Hess, N.; Oostrom, M.; Wietsma, T; Wand Valocchi, A. J.; Fouke, B. W.; Werth, C. *Environ. Sci. Technol.* **2010**, *44* (20), 7833−7838.

(7) Nnambi, I.; Werth, C.; Sanford, R.; Valocchi, A. *Environ. Sci. Technol.* **2003**, *37*, 5617−5624.

(8) Knutson, C.; Werth, C.; Valocchi, A. *Water Resour. Res.* **2005**, *41*, W07007.

(9) Aucour, A.-M.; Taoa, F.-X.; Moreira-Turcqb, P.; Seylerc, P.; Sheppardd, S.; Benedetti, M. *Chem. Geol.* **2003**, *197*, 271−285.

(10) Cirpka, O.; Frind, R.; Oand Helming, E. *J. Contam. Hydrol.* **1999**, *40*, 159−182.

(11) Raje, D. S.; Kapoor, V. *Environ. Sci. Technol.* **2000**, *34* (7), 1234−1239.

(12) Jose, S. C.; Cirpka, O. A. *Environ. Sci. Technol.* **2004**, *38* (7), 2089−2096.

(13) Rezaeia, M.; Sanz, E.; Raeisia, E.; Ayora, C.; Vasquez-Suñe, E.; Carrera, J. *J. Hydrol.* **2005**, *311*, 282−298.

(14) Weeks, C. W.; Sposito, G. *Water Resour. Res.* **1998**, *34*, 3315−3322.

(15) Gramling, C. M.; Harvey, C. F.; Meigs, L. C. *Environ. Sci. Technol.* **2002**, *36* (11), 2508−2514.

(16) De Simoni, M.; Carrera, J.; Sanchez-Vila, X.; Guadagnini, A. *Water Resour. Res.* **2005**, *41*, W11410 DOI: 10.1029/2005WR004056.

(17) Kapoor, V.; Gelhar, L. *Water Resour. Res.* **1994**, *30* (6), 1775−1788.

(18) Sanchez-Vila, X.; Guadagnini, D.; Fernàndez-Garcia, A. *Math. Geosci.* **2009**, *41*, 323−351, DOI: 10.1007/s11004-008-9204-2.

(19) Kitanidis, P. K. *Water Resour. Res.* **1994**, *30* (7), 2011−2026.

(20) Le Borgne, T.; Dentz, M.; Bolster, D.; Carrera, J.; Dreuzy, J.-R.; Davy, P. *Adv. Water Resour.* **2010**, *33* (12), 1468−1475.

(21) Fernàndez-Garcia, D.; Sanchez-Vila, X.; Guadagnini, A. *Adv. Water Res.* **2008**, *31*, 1364−1376.

(22) Luo, J.; Dentz, M.; Carrera, J.; Kitanidis, P. *Water Resour. Res.* **2008**, *44* (2), W02416 DOI: 10.1029/2006WR005658.

(23) McNeil, J.; Oldenborger, G.; Schincariol, R. *J. Contam. Hydrol.* **2006**, *84*, 39−54.

(24) Rahman, A.; S., J.; W., N.; Cirpka, O. *J. Contam. Hydrol.* **2005**, *80*, 130−148.

(25) Schincariol, R.; Herderick, E.; Schwartz, F. *J. Contam. Hydrol.* **1993**, *12*, 197−215.

(26) Konz, M.; Ackerer, P.; Meier, E.; Huggenberger, P.; Zechner, E.; Gechter, D. *Hydrol. Earth Syst. Sci.* **2008**, *12*, 727−738.

(27) Swartz, C. H.; Schwartz, F. W. *J. Contam. Hydrol.* **1998**, *34*, 169−189.

(28) *Smoothing Techniques, with Implementation in S*; York, H. N., Ed.; Springer Verlag, 1991.

(29) Takeda, H.; Farsiu, S.; Milanfar, P. *IEEE Trans. Acoust., Speech, Signal Process.* **2007**, *16*, 349−366.

(30) Fernàndez-Garcia, D.; Sanchez-Vila, X. *J. Contam. Hydrol.* **2011**, *120−121*, 99−114.

(31) Engel, J.; Herrmann, E.; Gasser, T. *Nonparametric Stat.* **1994**, *4*, 21−34.

(32) Wand, M.; Jones, M. *Comput. Stat.* **1994**, *9*, 97−116.

(33) Willmann, M.; Carrera, J.; Sanchez-Vila, X.; Silva, O.; Dentz, M. *Water Resour. Res.* **2010**, *46*, W07512 DOI: 10.1029/2009WR007739.

(34) Corbella, M.; Ayora, E.; Cardellach, E. *Miner. Deposita* **2004**, *39* (3), 344−357.

(35) Lachassagne, P.; Wyns, R.; Dewandel, B. *Terra Nova* **2011**, *23* (3), 145−161.